COMMUNICATIONS PHYSICS

ARTICLE

Spin torque nano-oscillator driven by combined spin injection from tunneling and spin Hall current

M. Tarequzzaman[1,2], T. Böhnert[1], M. Decker[3], J.D. Costa[1], J. Borme[1], B. Lacoste[1], E. Paz[1], A.S. Jenkins [1], S. Serrano-Guisan[1], C.H. Back[3], R. Ferreira[1] & P.P. Freitas[1,2]

Spin-transfer torque nano-oscillators (STNO) are important candidates for several applications based on ultra-tunable microwave generation and detection. The microwave dynamics in these STNOs are induced by spin currents that are typically generated either by spin polarization in an adjacent ferromagnetic layer or through the spin Hall effect. In this paper, a 3-terminal STNO based on a magnetic tunnel junction is excited by both of these spin injection mechanisms. The combination of these two mechanisms excites the free layer into dynamic regimes beyond what can be achieved by each excitation mechanism individually, resulting in enhanced output powers, a key figures of merit for device performance. The system response can be coherently quantified as a function of the total injected spin current density. The experimental data shows an excellent consistency with this simple model and a critical spin current density of $4.52 \pm 0.18 \times 10^9 \hbar/2\ e^{-1}\ Am^{-2}$.

[1] International Iberian Nanotechnology Laboratory (INL), Ave. Mestre Jose Veiga, 4715-330 Braga, Portugal. [2] Physics Department, Instituto Superior Tecnico (IST), Universidade de Lisboa, 1000–029 Lisbon, Portugal. [3] Institut für Experimentelle Physik, Universität Regensburg, D-93040 Regensburg, Germany. Correspondence and requests for materials should be addressed to T.B. (email: tim.boehnert@inl.int)

Spin torque nano-oscillators (STNOs) based on the spin-transfer torque (STT) associated with net spin currents are important candidates for several applications including frequency signal generation[1], signal modulation[2], spin wave generation[3], neuromorphic computing[4] and ultra-tunable microwave generators[5–8]. Such devices are conventionally manufactured from spin valve or magnetic tunnel junction (MTJ) stacks nanofabricated in different geometries, including nano-contacts[9–11] and nanopillars[12–14]. In the early years of the field, all these devices were excited into an auto-oscillatory state using a spin-polarized current injected in the free layer after being spin-polarized by the reference layer. This mechanism of excitation is particularly challenging for devices based on MTJ stacks since the large currents required to excite auto-oscillations are often large enough to irreversibly damage the devices. The onset of the dynamic effects in MTJ devices can only be observed if the tunneling spin current exerts a torque in the free layer that compensates the Gilbert damping. For in-plane ferromagnetic free layers, this condition can be expressed as[15]:

$$\eta J_{c,crit}^{tunneling} \hbar/2 \, e^{-1} = 2\mu_0 M_s \alpha t(M_{eff}/2 + H_{app}). \quad (1)$$

Here, μ_0 is the permeability of free space, $\hbar$ is the reduced Planck constant, M_s is the free layer saturation magnetization, α is the Gilbert damping constant, t is the thickness of the free layer, H_{app} is the applied field along easy axis, $J_{c,crit}^{tunneling}$ is the critical tunneling current density and η is the spin injection efficiency associated with the injection of the spin-polarized tunneling current from the reference layer into the free layer. The effective magnetization of the free layer is given by $M_{eff} = (M_s - 2K_p/(\mu_0 M_s))$ with the perpendicular magnetic anisotropy (K_p)[16,17].

The injected spin-polarized tunneling current in the free layer is limited by the voltage that can be sustained by the tunnel barrier before irreversible dielectric breakdown. Achieving the onset of dynamic auto-oscillations before the dielectric breakdown of the tunnel barrier requires a large spin injection efficiency η, which is related to the tunneling current polarization p by $\eta = p/(2 + 2p^2 \cos \varphi)$ with $\varphi = 0°$ in the low resistance configuration and $\varphi = 180°$ in the high resistance configuration[18,19]. Realizing nano-oscillators from stacks incorporating ultra-thin tunnel barriers is required in order to increase the maximum current sustained by the devices, but as the MgO becomes thinner the tunnel magnetoresistance (TMR) and p tend to decrease. Balancing these two effects is required to realize devices that can sustain large DC currents for long periods of time[13]. This particularly rigid requirement of STNOs is not shared with non-volatile magnetic memory (magnetoresistive random-access memory (MRAM)) devices which can be switched with short current pulses of large amplitude.

An important breakthrough was achieved using the spin Hall effect (SHE)[20,21] which generates transverse spin currents in non-magnetic materials such as Pt[22,23], Ta[24–27] and W[28,29] and also compensates the effective damping. The SHE was subsequently used in two-terminal devices to induce persistent auto-oscillations in the ferromagnetic layer[30–36] or even switch the ferromagnetic layer completely[24,37,38]. Later, the pioneering work of Liu et al.[6] induced auto-oscillations using the SHE in a three-terminal device based on an MTJ. While there are already a significant number of reports concerning three-terminal MRAM devices, the number of papers employing spin Hall currents as an excitation mechanism for auto-oscillations in MTJ nanopillars is very scarce[6,39] and the output powers achieved in such devices are considerably lower than those achieved in devices where the auto-oscillations are induced by spin-polarized tunneling currents. The likely reason for this discrepancy is the low charge to spin conversion ratio. Although the adjacent spin Hall materials do not

suffer dielectric breakdown, the current densities that they can sustain are limited by the electromigration[40].

An MTJ nanopillar was fabricated on a Ta micro-stripe adjacent to the free layer and measured in a three-terminal geometry with independent control of the tunneling current and the spin Hall charge current. In such device, it is possible to combine both types of excitations, concurrently injecting a spin-polarized tunneling current together with a transverse spin current generated by the SHE and driving the free layer into an auto-oscillation dynamic regime before any destructive mechanism is manifested (tunnel barrier breakdown or Ta line electromigration). For this reason, combining both spin injection mechanisms can result in spin current densities that are beyond those achievable with each isolated mechanism, allowing the exploration of otherwise unreachable dynamic states.

To describe this experiment, a more general version of Eq. 1 is necessary. The onset of auto-oscillation in the free layer is reached when the left-hand side of the Eq. 1 is replaced by the total critical injected spin current density, which is the sum of both contributions:

$$J_s = J_s^{tunneling} + J_s^{spin Hall} = \left(\eta J_c^{tunneling} + \theta J_c^{spin Hall}\right)\hbar/2 \, e^{-1}. \quad (2)$$

Here, $J_c^{tunneling}$ and $J_c^{spin Hall}$ are the tunneling and the spin Hall charge currents and $J_s^{tunneling}$ and $J_s^{spin Hall}$ are their respective spin currents.

In this work, it is shown that both excitation sources can be combined to drive the free layer into auto-oscillations that exceed the output power obtained with each individual input current within the limits that prevent irreversible damage to the device (from barrier breakdown or Ta electromigration). Furthermore, it is shown that Eq. 2 quantitatively describes a system with concurrent spin injection, providing a coherent description of spin injection in the free layer regardless of the excitation mechanism (tunneling charge current or spin hall charge current).

Results

Sample geometry and experimental details. In order to quantify the injected spin current density using Eq. 2, the parameters θ and η must be known. The spin Hall angle θ was quantified from separate stacks consisting of a 10 Ta/3 $Co_{0.4}Fe_{0.4}B_{0.2}$/5 MgO (thicknesses in nanometre). From these samples, θ was quantified by modulation of the effective damping of an adjacent ferromagnet[32,41,42], measured using the time-resolved magneto-optic Kerr effect. A spin Hall angle θ of (2.4 ± 0.1) % was computed as described in detail in the Supplementary Note 1.

The spin injection efficiency η was estimated from the TMR value in the final devices[43]. These were made from MTJ nanopillars with a diameter of 200 nm, patterned on a Ta spin Hall micro-stripe (see Methods section) as shown in Fig. 1a. A stack of 15 Ta/1.4 $Co_{0.4}Fe_{0.4}B_{0.2}$/MgO/2.2 $Co_{0.4}Fe_{0.4}B_{0.2}$/0.85 Ru/ 2.0 $Co_{0.7}Fe_{0.3}$/20 $Ir_{0.2}Mn_{0.8}$/5 Ru (thickness in nanometre) was used. The MgO thickness was tuned to a resistance-area product ($R \times A$) of 15 $\Omega \, \mu m^2$, previously found as an optimum value to maximize the output power of STNOs with auto-oscillations excited from spin-polarized currents[13]. The devices, measured in a four-contact point geometry curves with magnetic field sweeps along the reference layer magnetization, exhibit quasi-DC transfer curves which are consistent with an in-plane magnetization of the 1.4 nm thick $Co_{0.4}Fe_{0.4}B_{0.2}$ free layer. The free layer saturation magnetization M_s is determined from the saturation field of a magnetic film of the same thickness[44]. The measured $R \times A$ distribution in the final devices is shown in Fig. 1b with the large majority of the devices exhibiting a TMR between 100% and 120%. From the materials point of view, the large TMR of these devices is the key difference with respect to prior works[6,39]
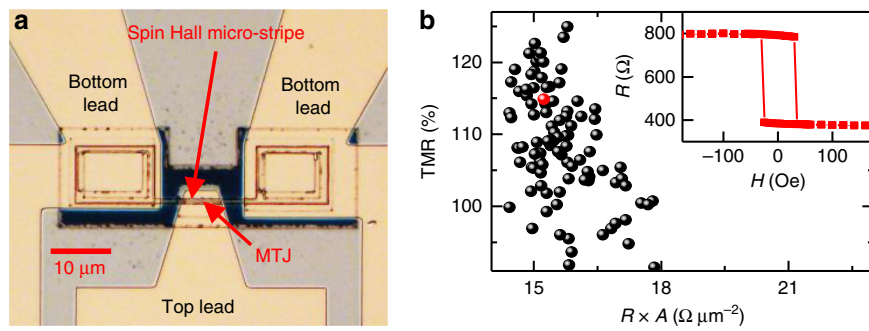
Fig. 1 Sample overview. a Optical microscope image of the final device. **b** Distribution of tunnel magnetoresistance (TMR) and resistance-area product ($R \times A$) measured in a 4-point geometry of a population of nanopillars with a diameter of 200 nm. The insert shows the 4-point transfer curve of a typical device
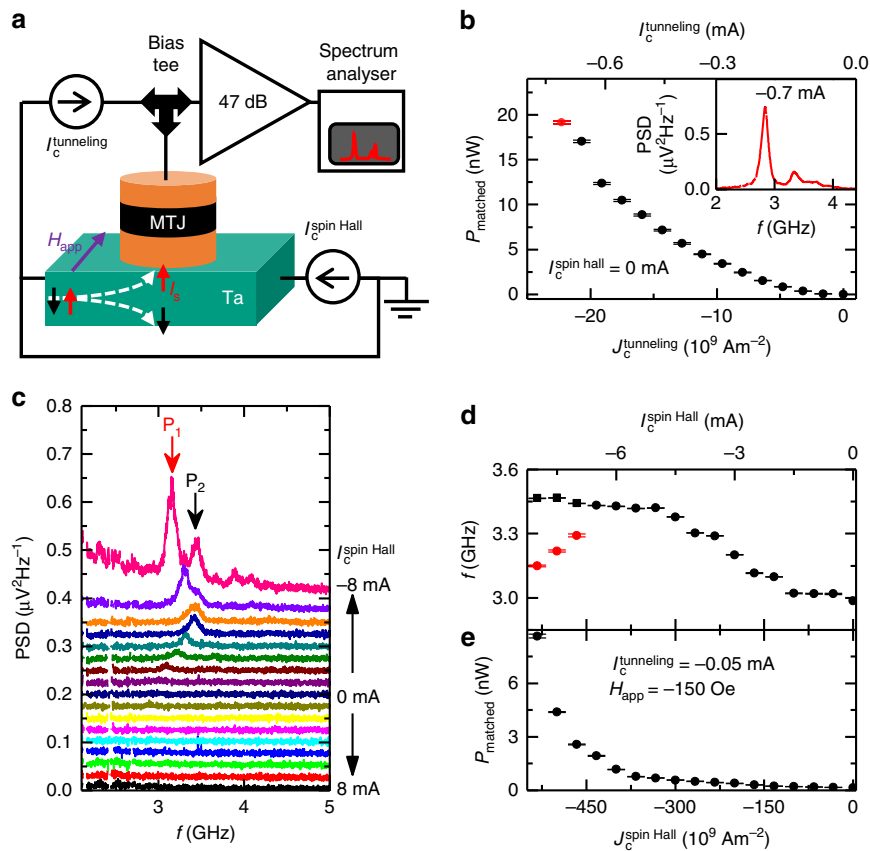

Fig. 2 The high-frequency response characterized in a 3-terminal configuration. a Schematic representation of the microwave emission measurement circuit setup for spin-polarized current-induced nano-oscillator devices. **b** Matched output power ($P_{matched}$) as a function of the tunneling current density ($J_c^{tunneling}$) in the absence of a spin Hall current ($I_c^{spin Hall}$). The inset shows the power spectral density (PSD) obtained at $I_c^{tunneling} = -0.7$ mA. **c** The PSD measured for $I_c^{spin Hall}$ ranging from +8 mA to −8 mA at a constant $I_c^{tunneling}$ of −50 µA and applied magnetic field of $H_{app} = -150$ Oe. The red squares indicate the second auto-oscillating mode (P_1 peak). The P_1 and P_2 peaks were fitted and included in the integrated power. **d**, **e** Frequency (f) and $P_{matched}$ as a function of $J_c^{spin Hall}$. The error bars in this figure represent the standard deviation of the fitting parameters of the Lorentz fit to the observed oscillation peaks

enabling the concurrent spin injection to be explored. With a TMR value of 115%, a tunneling current spin polarization p of 60% is estimated.

Tunneling current STT and spin Hall current STT. The high-frequency response of the devices was characterized in a three-terminal configuration for each excitation mechanism independently, as shown in Fig. 2a. The three-terminal configuration allows an independent control of spin Hall charge current ($I_c^{spin Hall}$) through the Ta layer and the tunneling charge current

($I_c^{tunneling}$) through the MTJ nanopillar. The $I_c^{tunneling}$ covered the range of ±0.7 mA ($J_c^{tunneling} = \pm 22.3 \times 10^9$ Am^{-2}), while $I_c^{spin Hall}$ was swept between ± mA ($J_c^{spin Hall} = \pm 333.3 \times 10^9$ Am^{-2}). During the experiments, an external magnetic field (H_{app}) of −150 Oe was applied to set the nanopillar in the anti-parallel (AP) state.

Firstly, the values of the tunneling current $I_c^{tunneling}$ were swept keeping the charge current in the adjacent Hall line at zero as shown in Fig. 2b. The power spectral density shows a peak at ~2.8 GHz with an output power that increases with increasingly
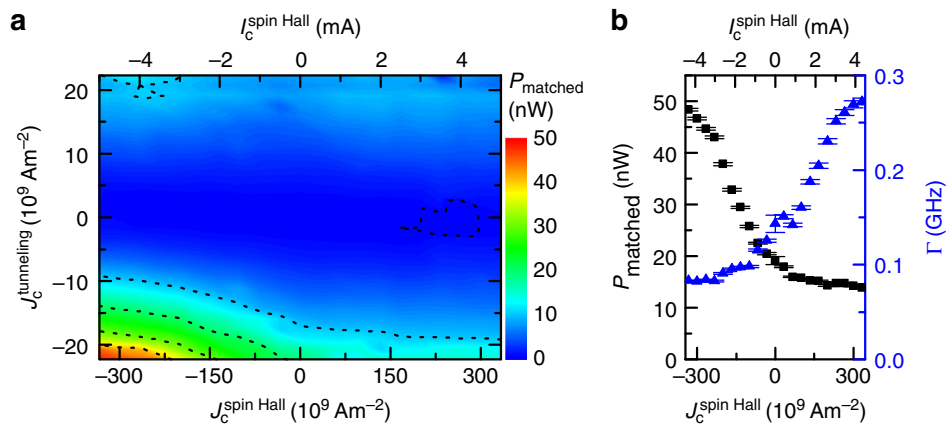
Fig. 3 Evaluation of the integrated output power due to the combined excitation sources. **a** Color map shows the integrated matched output power ($P_{matched}$) due to the combined excitation by the tunneling current density $\left(J_c^{tunneling}\right)$ and the spin Hall current density $\left(J_c^{spin\,Hall}\right)$. The black dashed lines represent the contour lines of equal power. **b** $P_{matched}$ and linewidth (Γ) as a function of $J_c^{spin\,Hall}$ at $J_c^{tunneling} = -22.3 \times 10^9$ Am^{-2} ($I_c^{tunneling} = -0.7$ mA) and fixed magnetic field $H_{app} = -150$ Oe. The error bars in this figure represent the standard deviation of the fitting parameters of the Lorentz fit to the observed oscillation peaks

negative charge current through the tunnel barrier, as shown in Fig. 2b. This polarity of the tunneling current corresponds to electrons tunneling from the fixed layer to the free layer. The observed auto-oscillation peak was fitted and integrated to obtain the matched output power ($P_{matched}$) and then corrected for the impedance mismatch of the circuit[13,44]. At the highest probed negative $I_c^{tunneling}$, free layer auto-oscillations with $P_{matched} = 19$ nW and a linewidth (Γ) of 100 MHz are observed. Larger amplitude currents cannot be injected without risking the irreversible breakdown or degradation of the tunnel barrier. Both $P_{matched}$ and Γ measured in this device are consistent with the values reported in the literature for the auto-oscillations of in-plane magnetized homogeneous nano-oscillators based on CoFeB/MgO/CoFeB MTJ stacks[45].

The auto-oscillations are observed for currents of negative polarity with an amplitude above a critical value of about -0.15 mA, corresponding to a tunneling current density of $J_c^{tunneling} = -4.65 \times 10^9$ Am^{-2}. Compared with the parameters found in the literature, this critical current density for the onset of auto-oscillations is low[46]. This is a consequence of the thin free layer, which leads to a low critical current density according to Eq. 1, together with the relatively large MgO barrier thickness leading[47] to a large TMR and spin polarization, which also contributes to decrease the critical current density as reported recently[13]. However, the threshold for auto-oscillations is difficult to determine precisely from the data in Fig. 2. A more precise discussion of the critical threshold takes place in the section on the determination of the critical spin current.

In a second experiment, shown in Fig. 2c–e, the magnetic auto-oscillations were excited by a spin Hall current. To that end, a weak tunneling current ($I_c^{tunneling} = -50$ μA) was applied and the frequency spectrum of the nano-oscillator was acquired while sweeping the DC charge current $I_c^{spin\,Hall}$ in the adjacent Ta line from 0 mA to ± 8 mA.

Using Eq. 2, the values for θ and η obtained from the experiments and the previously determined critical tunneling current, an estimated $J_c^{spin\,Hall} = -46 \times 10^9$ Am^{-2} is required to excite auto-oscillations in the free layer. Indeed, auto-oscillations are observed experimentally for all curves with larger negative $J_c^{spin\,Hall}$ values, as shown in Fig. 2c. No auto-oscillation peaks are observed for positive $J_c^{spin\,Hall}$ values. This excludes merely thermal

excitations of the ferromagnetic resonance (FMR) as discussed in the literature[6]. However, the very low bias current in this experiment results in small output powers and much lower signal-to-noise ratio.

Besides the critical current, $P_{matched}$ and f were also extracted in this experiment as a function of the charge current in the Ta line, as shown in Fig. 2d, e. The auto-oscillation peak in the power spectral density increases with increasing magnitude of negative $J_c^{spin\,Hall}$, as expected. At $J_c^{spin\,Hall}$ values greater than -6 mA, multiple auto-oscillating modes are detected. The two largest peaks (P_1 and P_2) are fitted and included in the integrated power. The peak P_1 is only observed above $I_c^{spin\,Hall} = -6$ mA and the associated frequency (red squares) can be seen in Fig. 2d. In the STT auto-oscillation regime, a typical red-shift[6] of the frequency is observed as the magnitude of $I_c^{spin\,Hall}$ increases. At large $J_c^{spin\,Hall}$ values, the $P_{matched}$ reaches 8.6 nW as shown in Fig. 2e. This power is 5 times larger than the values reported in the literature[5,6,31,48,49] for spin torque oscillators based on SHE (both in nanopillar and nano-constriction geometries). This improvement over previous three-terminal devices[6] was mostly due to a 5 times larger $J_c^{spin\,Hall}$ passed through Ta Hall micro-stripe which increases the total spin current accordingly. This is the maximum charge current that can be passed in the Ta line before irreversible damage to the line is observed.

Concurrent spin injection. After demonstrating the excitation of free layer auto-oscillation in the same nanopillar by either a tunneling current or a transverse spin current, the next step is to combine both spin injection methods. The output power spectrum was acquired while $I_c^{spin\,Hall}$ and $I_c^{tunneling}$ are both swept. The integrated output power of the observed precession peaks are shown in Fig. 3a for all values of the two currents. The results reproduce the trends observed with each isolated excitation: the magnitude of the auto-oscillations increases with increasingly negative $I_c^{tunneling}$ as well as increasingly negative $I_c^{spin\,Hall}$. By simultaneously exciting the free layer with $I_c^{tunneling} = -0.7$ mA and $I_c^{spin\,Hall} = -5$ mA, a $P_{matched}$ of 48 nW and a minimum Γ of 83 MHz are obtained, which exceeds the $P_{matched}$ obtained with either a pure tunneling current or a pure spin Hall current within the limits that prevent irreversible degradation of the tunnel barrier or Ta line.

Figure 3b displays $P_{matched}$ and Γ as a function of $J_c^{spin\,Hall}$ for a fixed value of $J_c^{tunneling} = -22.3 \times 10^9\,\mathrm{Am^{-2}}$ ($I_c^{tunneling} = -0.7$ mA). Unlike the previous spin Hall current measurement with low $I_c^{tunneling} = -50\,\mu\mathrm{A}$ (Fig. 2c–e), this value of the tunneling current is large enough to generate free layer auto-oscillations at zero $J_c^{spin\,Hall}$. The $J_c^{spin\,Hall}$ will either act with or against the tunneling spin current and, thus, either reinforces or damps the auto-oscillations depending on the polarity. As $J_c^{spin\,Hall}$ is swept from zero to a maximum negative value, the $P_{matched}$ increases due to the increase of the total spin current in the system, as expected from the theoretical models[50,51]. For positive $J_c^{spin\,Hall}$, $P_{matched}$ initially reduces, before leveling out at an almost constant power of 13.8 nW with $\Gamma > 200$ MHz, which corresponds to the thermal FMR.

An alternative interpretation of the data in Fig. 3 could be that the increased output power is related to an increase of the average MTJ temperature[52,53] for high $J_c^{spin\,Hall}$ and $J_c^{tunneling}$ values. Especially as the larger $I_c^{spin\,Hall}$ will generate a large Joule heating in the highly resistive Ta line. From finite element simulations and additional experiments (see Supplementary Note 2) the dominating origin of the output power is clearly the spin current. However, with increasing $I_c^{spin\,Hall}$ values the average temperature does increase, contributing in some part to the increase of the output power. It is estimated that at $J_c^{spin\,Hall}$ of $\pm 333.3 \times 10^9\,\mathrm{m^{-2}}$ and $J_c^{tunneling}$ of $20.0 \times 10^9\,\mathrm{Am^{-2}}$, about 24% of the total output power is due to the elevated temperature of the MTJ. Although noticeable, thermal effects are not dominant. More complex mechanisms such as the Seebeck effect[54] or the spin Seebeck effect[53,55,56] can be neglected in this experiment. According to the simulations the temperature difference across the junction is around 1 K, and thus the resulting thermal current is expected to be several orders of magnitudes below the applied bias current.

Critical spin current determination. A coherent and quantitative description of the system can be obtained with the spin current density defined in Eq. 2. In order to determine the critical spin current (J_s) of the device, at first, the thermal FMR power at the positive spin Hall current values were subtracted from the $P_{matched}$ to determine the STT-dependent contributions (P_{STT}). For additional details see Supplementary Note 3. The resulting matched root mean square (rms) microwave power P_{STT} can be described by the following equation[7,57].

$$P_{STT} = I^2 \Delta R^2 / (32R),\qquad(3)$$

with the applied tunneling current I and the static resistance of the device R, which is approximately the MTJ resistance in the AP state. The observed microwave power results from the resistance oscillation ΔR due to the magnetization auto-oscillation of the free layer. The factor 32 results from the combination of a factor of 8 due to the peak-to-peak to rms conversion and a factor of 4 due to the power splitting in a matched circuit. The normalized auto-oscillation amplitude can finally be expressed as a ratio between ΔR and $\Delta R_{max} = R_{AP} - R_P$ as expressed by:

$$\Delta R / \Delta R_{max} = \sqrt{32 R P_{STT}} / (I \Delta R_{max}).\qquad(4)$$

Expressing the auto-oscillation in the normalized amplitude $\Delta R/\Delta R_{max}$, rather than P_{STT}, allows the direct comparison of all the spin current configurations since this normalization accounts for the remaining tunneling current dependencies. Note that ΔR_{max} and η were determined as a function of $J_c^{tunneling}$ to remove the influence of the decreasing TMR ratio. Any value of $\Delta R/\Delta R_{max}$ describes a certain excitation amplitude and the contours lines in

Fig. 4a visualizes the point of equal excitation at varying $J_c^{spin\,Hall}$ and $J_c^{tunneling}$. The slopes of these contour lines correspond to the ratio of θ/η with the previously obtained value of $\theta = 2.4\%$ and the η values between 44% and 28% (see Supplementary Note 4). Thus, the relation given by Eq. 2 seems to be valid and can be used to convert the charge current densities into J_s values. The ratio $\Delta R/\Delta R_{max}$ can be now expressed as a function of J_s, as shown in Fig. 4b.

The consistency of results of the same J_s with varying tunneling and spin Hall contributions clearly shows that both $J_c^{tunneling}$ and $J_c^{spin\,Hall}$ contribute to the STT and can be described by Eq. 2. It should be emphasized that only a correct ratio of θ/η leads to the presented relation and any deviations would lead to a significant spread from the observed homogenous behavior in Fig. 4b. In the proximity of the critical spin current density ($J_{s,\,crit}$) the ratio $\Delta R/\Delta R_{max}$ is predicted to be equal to $p_0 = (J_s - J_{s,crit})/(J_s + J_{s,crit} \cdot Q)$, with the non-linear damping constant Q[58,59]. This prediction describes the result very well and the fit results in $J_{s,\,crit} = -4.52 \pm 0.18 \times 10^9 \hbar/2\,e^{-1}\,\mathrm{Am^{-2}}$ and a non-linear damping $Q = 3.8 \pm 0.3$ which is comparable to the literature[59]. Both error values are the standard deviation resulting from the fit shown in Fig. 4b. From Eq. 1 a damping constant of 0.0083 ± 0.001 is determined for a nominal nanopillar diameter of 200 nm. This standard deviation includes an error due to the deviation from the nominal diameter of the device of about 10%. This value is in the same range as the damping constant of 0.00745 ± 0.00007 determined independently in the spin Hall angle measurement (see Supplementary Note 1) and in literature[25,60]. The combinations of $J_c^{tunneling}$ and $J_c^{spin\,Hall}$ that result in spin currents of $J_{s,\,crit}$ are indicated by the red line in Fig. 4a. The normalized auto-oscillation amplitude $\Delta R/\Delta R_{max}$ describes the excitation directly and excludes unrelated effects such as the bias dependence of the polarization or the bias dependence of the output power. Although the output power remains a central parameter for applications, this normalized auto-oscillation amplitude is crucial for a quantitative analysis.

The Γ as a function of J_s decreases with increasing auto-oscillation amplitude, as shown in Fig. 4c, which is typical for auto-oscillatory behavior and in agreement with the previous reports[61]. However, f shows a blue-shift with increasingly negative J_s and an additional spread of the data. This spread is linearly related to the currents in the system, $I_c^{tunneling}$ and $I_c^{spin\,Hall}$, as shown in Fig. 4d. This perturbation could be related to effects such as radial Oersted field in the nanopillar[62], voltage-controlled anisotropy changes[6], field-like torques[63], lateral Oersted field around the Ta line[31] and temperature effects[15,30]. Thus, the true frequency shift cannot be distinguished with certainty from these additional effects. As a result, the observed frequency spread cannot be compared to the predicted red-shift[15]. It is interesting to note that the amplitude of the excitation does not show a similar spread and only depends on the J_s.

Discussion
A three-terminal STNO based on an MTJ stack patterned into nanopillars with an adjacent Ta line acting as a transverse spin current source was realized. This MTJ stack exhibits a large TMR ratio (~115%) and a tunnel barrier of intermediate thickness allowing an excitation of free layer auto-oscillations by spin injection from a tunneling current, a transverse spin Hall current or a combination of both injection methods. Earlier works that explored comparable stacks and geometries did not demonstrate the ability to promote auto-oscillations of the free layer by both effects in the same device[6].
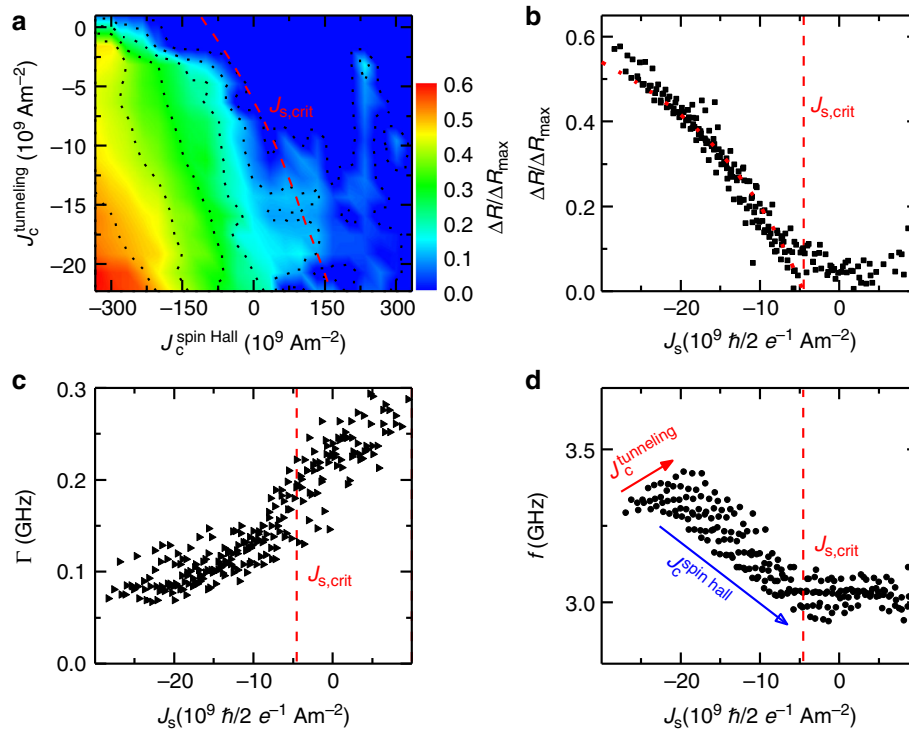
Fig. 4 Evaluation of normalized oscillation parameter and fit to theory. **a** Color map of the normalized auto-oscillation amplitude ratio ($\Delta R/\Delta R_{max}$). The slope of the contour lines of equal excitation corresponds to the ratio of θ/η. The red dashed line follows the combinations of the tunneling current density $\left(J_c^{tunneling}\right)$ and the spin Hall current density $\left(J_c^{spin\,Hall}\right)$ that result in the critical spin current($J_{s,crit}$). **b** The ratio $\Delta R/\Delta R_{max}$ versus the total spin current (J_s) in the magnetic tunnel junction determined by Eq. 2. $J_{s,crit}$ is determined from this fit. **c, d** Linewidth (Γ) and oscillation frequency (f) versus J_s displaying a certain spread of the data, which is related to $J_c^{tunneling}$ and $J_c^{spin\,Hall}$ in the experiment as indicated by the arrows (direction indicates an increase in value). Although different combination of $J_c^{tunneling}$ and $J_c^{spin\,Hall}$ result in the same oscillation amplitude, it seems that the two excitation sources result in different shift of f and to a smaller extend in a different Γ

The benefits of combining these two sources of excitations are simple. The total spin current injected in the free layer can be larger than what is possible from each isolated mechanism before irreversible damage arises (the tunneling current is limited by the tunnel barrier breakdown and the spin Hall current is limited by electromigration in the Ta line). Thus, the free layer can be excited in to dynamic states that are not accessible unless the two excitation sources are combined. This is clearly demonstrated in this paper when an output power of 48 nW is obtained with the two combined currents, well above the output power achieved with each individual excitation source.

Furthermore, the data exhibit an excellent quantitative agreement with theoretical models expressed as a function of the total spin current injected into the free layer. The spin current can be calculated from the applied tunneling current and the applied spin Hall current and is used to predict the critical spin current of the system. The quantitative model confirms the values of key parameters in the system, such as the spin polarization of the tunneling current η and the spin Hall angle θ.

Methods

STNO fabrication. The stack (15 Ta/1.4 $Co_{0.4}Fe_{0.4}B_{0.2}$/MgO/2.2 $Co_{0.4}Fe_{0.4}B_{0.2}$/0.85 Ru/2.0 $Co_{0.7}Fe_{0.3}$/20 $Ir_{0.2}Mn_{0.8}$/5 Ru (thickness in nanometre) was deposited over Si/100 nm Al_2O_3 substrate in physical vapor deposition system with a base pressure of 1×10^{-9} Torr. Nanopillars with a 200 nm diameter were patterned from the stack, incorporating a MgO barrier targeting a resistance-area product ($R \times A$) of 9.7 $\Omega\,\mu m^2$. Here a Ta layer was used as a seed layer for the growth of the MTJ stack and was pattered into a lead with the twofold function of establishing electrical contact to the bottom electrode of the MTJ nanopillars as well as constituting the current line converting the charge current into a transverse spin current being injected into the free layer.

The STNO fabrication can be segmented into three major parts: nanopillar patterning, bottom electrode definition and planarization. The electron beam

lithography (EBL) was used to define the nanopillar and bottom electrode and the direct write laser lithography was used to define the top electrode of the device. Throughout nanofabrication process, ion beam etching was used for all the etching purpose.

At first, the nanopillar patterning was done using conventional EBL followed by etching in ion beam milling. The secondary ion mass spectrometer which is incorporated with the etching system was used to monitor the etching process. A negative photoresist (AZ7520) has been used for EBL exposure. Following the nanopillar patterning, another EBL was done to define a Hall bar structure of 24 μm long with a width of 1 μm using same photoresist. The length, width and height were chosen in order to ensure that the large $J_c^{spin\,Hall}$ can be reached in the Hall current micro-stripe with reasonable current values. Upon the bottom electrode definition, the nanopillar was buried into 600 nm Al_2O_3 and planarize in ion beam milling with grazing angle to expose the top of the nanopillar. The stopping point for this process was established by monitoring the evolution of the oxide topography on top of the nanopillar using scanning electron microscopy. The rest of the lithographies were performed in order to electrically contact the bottom electrode with the top electrode. A picture of a finished device is shown in Fig. 1a.

Upon nanofabrication, the devices were annealed at 330 °C, with a dwell time of 2 h and magnetic field of 1 T to pin the synthetic antiferromagnet of the reference layer. The free layer of these devices aligns with the applied magnetic field leading to a parallel configuration (P) with low electrical resistance in positive magnetic field direction and an anti-parallel configuration with high R in the negative magnetic field direction.

Concurrent spin injection setup. Two DC current sources with common ground were employed to independently control two currents: the spin Hall charge current $\left(I_c^{spin\,Hall}\right)$ through the Ta layer and the tunneling charge current $\left(I_c^{tunneling}\right)$ through the MTJ nanopillar. The high-frequency component of the output signal was then amplified by 43 dB and measured in a spectrum analyzer. To obtain the output power ($P_{matched}$), the power spectral density of the auto-oscillation peak is integrated and the impedance mismatch between the MTJ and the 50 Ω load is taken into account in order to calculate the output power delivered by the MTJ to the matched load[13,64]. Specifically, the following formula is used to convert the measured voltages into $P_{matched}$: $P_{matched} = P_{measured} (R_{MTJ} + R_L)^2/(4R_{MTJ}R_L)$. Where $P_{measured}$ is the integrated power measured in the spectrum analyzer, R_{MTJ} is

the resistance of the MTJ and R_L is the load resistance of the system. All output power values given in this work are corrected by this mismatch and represent the integrated (rms) output power delivered to a matched load. It should be noted that reported $P_{matched}$ is around 20% of the matched power of a circuit without the high resistive Ta lead, which dissipates a large amount of the generated power. These specific losses can be potentially decreased by optimizing design and materials. LabVIEW was used in this study to control, record and process data from the measurement setup.

Data availability

The data that support the findings of this study are available from the corresponding authors upon reasonable request.

References

1. Bankowski, E. et al. Magnonic crystal as a delay line for low-noise auto-oscillators. *Appl. Phys. Lett.* **107**, 122409 (2015).
2. Quinsat, M. et al. Modulation bandwidth of spin torque oscillators under current modulation. *Appl. Phys. Lett.* **105**, 152401 (2014).
3. Slavin, A. & Tiberkevich, V. Spin wave mode excited by spin-polarized current in a magnetic nanocontact is a standing self-localized wave bullet. *Phys. Rev. Lett.* **95**, 237201 (2005).
4. Torrejon, J. et al. Neuromorphic computing with nanoscale spintronic oscillators. *Nature* **547**, 428–431 (2017).
5. Ranjbar, M. et al. CoFeB-based spin Hall nano-oscillators. *IEEE Magn. Lett.* **5**, 3000504 (2014).
6. Liu, L., Pai, C. F., Ralph, D. C. & Buhrman, R. A. Magnetic oscillations driven by the spin Hall effect in 3-terminal magnetic tunnel junction devices. *Phys. Rev. Lett.* **109**, 186602 (2012).
7. Kiselev, S. I. et al. Microwave oscillations of a nanomagnet driven by a spin-polarized current. *Nature* **425**, 380–383 (2003).
8. Demidov, V. E. et al. Magnetic nano-oscillator driven by pure spin current. *Nat. Mater.* **11**, 1028–1031 (2012).
9. Sani, S. et al. Mutually synchronized bottom-up multi-nanocontact spin-torque oscillators. *Nat. Commun.* **4**, 2731 (2013).
10. Kaka, S. et al. Mutual phase-locking of microwave spin torque nano-oscillators. *Nature* **437**, 389–392 (2005).
11. Silva, T. J. & Rippard, W. H. Developments in nano-oscillators based upon spin-transfer point-contact devices. *J. Magn. Magn. Mater.* **320**, 1260–1271 (2008).
12. Houssameddine, D. et al. Spin transfer induced coherent microwave emission with large power from nanoscale MgO tunnel junctions. *Appl. Phys. Lett.* **93**, 022505 (2008).
13. Costa, J. D. et al. High power and low critical current density spin transfer torque nano-oscillators using MgO barriers with intermediate thickness. *Sci. Rep.* **7**, 7237 (2017).
14. Deac, A. M. et al. Bias-driven high-power microwave emission from MgO-based tunnel magnetoresistance devices. *Nat. Phys.* **4**, 803–809 (2008).
15. Stiles, M. D. & Miltat, J. Spin-transfer torque and dynamics. in. *Top. Appl. Phys.* **101**, 225–308 (2006).
16. Wang, W. X. et al. The perpendicular anisotropy of Co40Fe40B20 sandwiched between Ta and MgO layers and its application in CoFeB/MgO/CoFeB tunnel junction. *Appl. Phys. Lett.* **99**, 148–151 (2011).
17. Dieny, B. & Chshiev, M. Perpendicular magnetic anisotropy at transition metal/oxide interfaces and applications. *Rev. Mod. Phys.* **89**, 02008 (2017).
18. Slonczewski, J. C. Currents, torques, and polarization factors in magnetic tunnel junctions. *Phys. Rev. B* **71**, 024411 (2005).
19. Diao, Z. et al. Spin transfer switching and spin polarization in magnetic tunnel junctions with MgO and AlO x barriers. *Appl. Phys. Lett.* **87**, 232502 (2005).
20. Hirsch, J. E. Spin Hall effect. *Phys. Rev. Lett.* **83**, 1834–1837 (1999).
21. Hoffmann, A. Spin Hall effects in metals. *IEEE Trans. Magn.* **49**, 5172–5193 (2013).
22. Dürrenfeld, P., Awad, A. A., Houshang, A., Dumas, R. K. & Åkerman, J. A 20 nm spin Hall nano-oscillator. *Nanoscale* **9**, 1285–1291 (2017).
23. Pai, C. F. et al. Dependence of the efficiency of spin Hall torque on the transparency of Pt/ferromagnetic layer interfaces. *Phys. Rev. B* **92**, 064426 (2015).
24. Liu, L. et al. Spin-torque switching with the giant spin Hall effect of tantalum. *Science* **336**, 555–558 (2012).
25. Jamali, M., Klemm, A. & Wang, J. P. Precessional magnetization induced spin current from CoFeB into Ta. *Appl. Phys. Lett.* **103**, 252409 (2013).
26. Gomez, J. E. et al. Spin transport parameters in Ni80Fe20/Ru and Ni80Fe20/Ta bilayers. *Phys. Rev. B* **90**, 064428 (2014).
27. Hahn, C. et al. Comparative measurements of inverse spin Hall effects and magnetoresistance in YIG/Pt and YIG/Ta. *Phys. Rev. B* **87**, 174417 (2013).
28. Pai, C. F. et al. Spin transfer torque devices utilizing the giant spin Hall effect of tungsten. *Appl. Phys. Lett.* **101**, 122404 (2012).
29. Hao, Q., Chen, W. & Xiao, G. Beta (β) tungsten thin films: structure, electron transport, and giant spin Hall effect. *Appl. Phys. Lett.* **106**, 182403 (2015).
30. Demidov, V. E., Urazhdin, S., Zholud, A., Sadovnikov, A. V. & Demokritov, S. O. Nanoconstriction-based spin-Hall nano-oscillator. *Appl. Phys. Lett.* **105**, 172410 (2014).
31. Awad, A. A. et al. Long-range mutual synchronization of spin Hall nano-oscillators. *Nat. Phys.* **13**, 292–299 (2016).
32. Ando, K. et al. Electric manipulation of spin relaxation using the spin hall effect. *Phys. Rev. Lett.* **101**, 036601 (2008).
33. Evelt, M. et al. Spin Hall-induced auto-oscillations in ultrathin YIG grown on Pt. *Sci. Rep.* **8**, 1269 (2018).
34. Collet, M. et al. Generation of coherent spin-wave modes in yttrium iron garnet microdiscs by spin-orbit torque. *Nat. Commun.* **7**, 10377 (2016).
35. Wunderlich, J., Wunderlich., J. & Olejník, K. Spin Hall effect devices. *Nat. Mater.* **11**, 382–390 (2012).
36. Chen, T. et al. Spin-torque and Spin-hall nano-oscillators. *Proc. IEEE* **104**, 1919–1945 (2016).
37. Miron, I. M. et al. Perpendicular switching of a single ferromagnetic layer induced by in-plane current injection. *Nature* **476**, 189–193 (2011).
38. Wang, W.-G., Li, M., Hageman, S. & Chien, C. L. Electric-field-assisted switching in magnetic tunnel junctions. *Nat. Mater.* **11**, 64–68 (2011).
39. Jué, E., Pufall, M. R., Rippard, W. H., Pufall, M. R. & Rippard, W. H. Asymmetric and partial injection locking of a three-terminal spin-torque oscillator. *Appl. Phys. Lett.* **112**, 102403 (2018).
40. Slachter, A., Bakker, F. L., Adam, J. & Wees, B. J. Van. Thermally driven spin injection from a ferromagnet into a non-magnetic metal. *Nat. Phys.* **6**, 879–882 (2010).
41. Liu, L., Moriyama, T., Ralph, D. C. & Buhrman, R. A. Spin-torque ferromagnetic resonance induced by the spin Hall effect. *Phys. Rev. Lett.* **106**, 036601 (2011).
42. Kasai, S. et al. Modulation of effective damping constant using spin Hall effect. *Appl. Phys. Lett.* **104**, 092408 (2014).
43. Fuchs, G. D. et al. Spin torque, tunnel-current spin polarization, and magnetoresistance in MgO magnetic tunnel junctions. *Phys. Rev. Lett.* **96**, 186603 (2006).
44. Tarequzzaman, M. et al. Broadband voltage rectifier induced by linear bias dependence in CoFeB/MgO magnetic tunnel junctions. *Appl. Phys. Lett.* **112**, 252401 (2018).
45. Purbawati, A. et al. Frequency shift keying by current modulation in a MTJ-based STNO with high data rate. *Appl. Phys. Lett.* **11**, 082401 (2017).
46. Zeng, Z., Finocchio, G. & Jiang, H. Spin transfer nano-oscillators. *Nanoscale* **5**, 2219 (2013).
47. Zeng, Z. et al. Ultralow-current-density and bias-field-free spin-transfer nano-oscillator. *Sci. Rep.* **3**, 1426 (2013).
48. Demidov, V. E. et al. Synchronization of spin Hall nano-oscillators to external microwave signals. *Nat. Commun.* **5**, 3179 (2014).
49. Liu, R. H., Lim, W. L. & Urazhdin, S. Spectral characteristics of the microwave emission by the spin Hall nano-oscillator. *Phys. Rev. Lett.* **110**, 147601 (2013).
50. Kim, J. V., Mistral, Q., Chappert, C., Tiberkevich, V. S. & Slavin, A. N. Line shape distortion in a nonlinear auto-oscillator near generation threshold: application to spin-torque nano-oscillators. *Phys. Rev. Lett.* **100**, 167201 (2008).
51. Slavin, A. & Tiberkevich, V. Excitation of spin waves by spin-polarized current in magnetic nano-structures. *Magn. IEEE Trans.* **44**, 1916–1927 (2008).
52. Pushp, A. et al. Giant thermal spin-torque–assisted magnetic tunnel junction switching. *Proc. Natl Acad. Sci. USA* **112**, 6585–6590 (2015).
53. Safranski, C. et al. Spin caloritronic nano-oscillator. *Nat. Commun.* **8**, 117 (2017).
54. Blundell, K., Stephen, J. & Blundell, K. M. *Concepts in Thermal Physics* (Oxford University Press, Oxford, 2009).
55. Uchida, K. et al. Observation of the spin Seebeck effect. *Nature* **455**, 778–781 (2008).
56. Agrawal, M. et al. Role of bulk-magnon transport in the temporal evolution of the longitudinal spin-Seebeck effect. *Phys. Rev. B* **89**, 224414 (2014).
57. Houssameddine, D. et al. Spin-torque oscillator using a perpendicular polarizer and a planar free layer. *Nat. Mater.* **6**, 447–453 (2007).
58. Tiberkevich, V., Slavin, A. & Kim, J. V. Microwave power generated by a spin-torque oscillator in the presence of noise. *Appl. Phys. Lett.* **91**, 192506 (2007).
59. Tiberkevich, V. & Slavin, A. Nonlinear phenomenological model of magnetic dissipation for large precession angles: generalization of the Gilbert model. *Phys. Rev. B* **75**, 014440 (2007).

60. Shinozaki, M. et al. Damping constant in a free layer in nanoscale CoFeB/MgO magnetic tunnel junctions investigated by homodyne-detected ferromagnetic resonance. *Appl. Phys. Express* **10**, 013001 (2017).

61. Wada, T. et al. Spin-transfer-torque-induced rf oscillations in CoFeB/MgO/CoFeB magnetic tunnel junctions under a perpendicular magnetic field. *Phys. Rev. B* **81**, 104410 (2010).

62. Devolder, T. et al. Temperature study of the spin-transfer switching speed from dc to 100 ps. *J. Appl. Phys.* **98**, 053904 (2005).

63. Guo, Y. Y., Xue, H., Bin & Liu, Z. J. Oscillation characteristics of zero-field spin transfer oscillators with field-like torque. *AIP Adv.* **5**, 057114 (2015).

64. Blyler, J., Ajluni, C. & Bowick, C. *RF Circuit Design* (Elsevier, New York, 2008).

Acknowledgements

Author contributions

R.F. and P.P.F. conceived the original idea for the study. M.T., E.P., J.B. and R.F. fabricated the devices. M.D. and C.H.B. characterized Ta lead. M.T. and T.B. characterized the oscillators with the help of J.D.C., B.L. and S.S.-G. R.F. and P.P.F. supervised the project. B.L. and A.S.J. provided the theoretical background of the work. All authors contributed to the interpretation of the data and to the writing of the manuscript.

Additional information

Supplementary information accompanies this paper at https://doi.org/10.1038/s42005-019-0119-7.

Competing interests: The authors declare no competing interests.

Reprints and permission information is available online at http://npg.nature.com/reprintsandpermissions/

Publisher's note: Springer Nature remains neutral with regard to jurisdictional claims in published maps and institutional affiliations.